LETTERS
PUBLISHED ONLINE: 22 AUGUST 2010 | DOI: 10.1038/NGEO943
nature geoscience

Significant sink of ocean-eddy energy near western boundaries

Xiaoming Zhai[1]*, Helen L. Johnson[2] and David P. Marshall[1]

Ocean eddies generated through instability of the mean flow are a vital component of the energy budget of the global ocean[1–3]. In equilibrium, the sources and sinks of eddy energy have to be balanced. However, where and how eddy energy is removed remains uncertain[3,4]. Ocean eddies are observed to propagate westwards at speeds similar to the phase speeds of classical Rossby waves[5], but what happens to the eddies when they encounter the western boundary is unclear. Here we use a simple reduced-gravity model along with satellite altimetry data to show that the western boundary acts as a 'graveyard' for the westward-propagating ocean eddies. We estimate a convergence of eddy energy near the western boundary of approximately 0.1–0.3 TW, poleward of 10° in latitude. This energy is most probably scattered into high-wavenumber vertical modes, resulting in energy dissipation and diapycnal mixing[6]. If confirmed, this eddy-energy sink will have important implications for the ocean circulation.

There is increasing evidence in support of the idea that the available potential energy built up by large-scale wind Ekman pumping of the main thermocline is released by the generation of eddies through instabilities of the mean currents[1–3]. Our understanding of the fate of these eddies is, however, rather speculative. There are a few candidate processes that may dissipate eddies in the ocean[3,4]. For example, drag at the ocean bottom[3,7] and suppression by the surface wind stress[8–12] provide direct mechanical damping of the eddies. Interactions between geostrophic eddies and internal waves through loss of balance[13] and Rossby wave deformation[14] may provide another route of energy leakage out of the eddy field. Eddies are also known to drive mean currents along sloping topography through the 'Neptune effect'[15,16]. A fraction of the eddy energy in the Southern Ocean may be transferred to internal lee waves and oscillations over rough bottom topography, leading to bottom-enhanced diapycnal mixing[17–19]. However, none of the above processes have been shown to provide the dominant eddy-energy sink. Where and how eddies are dissipated in the ocean is still an open and important question. If we know where it happens, this may give us clues as to how it does so.

Except in the Antarctic Circumpolar Current and separated Western Boundary Currents, oceanic eddies propagate ubiquitously westward at speeds similar to the phase speeds of classical Rossby waves[5]. What, then, happens to the eddies when they encounter the western boundary, and could this provide us a significant eddy-energy sink in the ocean? We first answer these questions by examining the eddy energy budget near the western boundary in a nonlinear reduced-gravity model (see Methods). The model[20,21] is solved on a β-plane, with a background layer thickness of 750 m, a reduced gravity of 0.015 $m^2\,s^{-1}$ and a lateral resolution of 3.5 km (equivalent to 1/32° in latitude).

We first conduct a model integration initialized with a single, anticyclonic eddy, avoiding the complication of eddy–eddy interactions. This eddy has a diameter of about 500 km, and a layer thickness anomaly of 130 m (equivalent to a sea-surface-height anomaly of 20 cm; Fig. 1a). The eddy propagates westward at a speed of about 5 $cm\,s^{-1}$, and its leading edge reaches the western boundary after three months (Fig. 1a–d). The region near the western boundary enclosed by the dashed–dotted line is where the eddy energy-budget analysis is conducted. Figure 1e shows the time series of the incoming eddy energy flux from the east (blue), meridional energy flux through the southern open boundary of the box (red) and eddy-energy dissipation within the box (black). For this single eddy, only about 7% of its initial energy escapes equatorward through the southern open boundary, and the majority is dissipated near the incident latitude within the box (Fig. 1e and f).

As a step toward a more realistic simulation, a second integration is conducted, initialized with a random sea of eddies (Fig. 2a). The eddies again propagate westward while interacting with one another and cascading energy to larger scales through the merging of eddies of the same parity (Fig. 2a–d). Figure 2e shows that the incoming eddy energy flux from the east, in the case of a sea of propagating eddies, is almost exactly balanced by the viscous dissipation in the control volume near the western boundary, with less than 2% of the incident energy leaking out of the equatorward edge of the box. The picture that emerges from our model study is as follows: the eddies propagate westward at the speed of long Rossby waves; on encountering the western boundary, the available potential energy associated with the eddies is converted into kinetic energy of the reflected short Rossby waves[22] and smaller eddies, the majority of which is viscously dissipated near the western boundary. In the ocean, it is likely that much of the eddy energy is scattered into high-wavenumber vertical modes that rapidly dissipate[6].

We now use satellite altimetry and climatological hydrographic data to map the divergence of eddy energy in the first baroclinic mode[23,24]. To compute the surface eddy energy fluxes, we use the surface geostrophic-velocity anomaly, $\mathbf{u}'$, for the period from January 1995 to December 2008 that is computed from the global sea-surface-height anomaly (η') dataset compiled by the CLS Space Oceanographic Division of Toulouse, France. The dataset merges the TOPEX/Poseidon and ERS-1/2 along-track sea-surface-height measurements to give temporal resolution of a week and spatial resolution of 1/3° in longitude[25]. The vertical structure of the eddy energy fluxes is determined from climatological hydrographic data[26] (see Methods).

The divergence of the depth-integrated linear eddy energy fluxes is

$$D = \nabla_h \cdot \left(\int_{-H}^{0} \overline{\mathbf{u}'_1 p'_1}\, \mathrm{d}z \right) \qquad (1)$$

[1]Atmospheric, Oceanic and Planetary Physics, University of Oxford, Oxford OX1 3PU, UK, [2]Earth Sciences, University of Oxford, Oxford OX1 3PR, UK.
*e-mail: zhai@atm.ox.ac.uk.

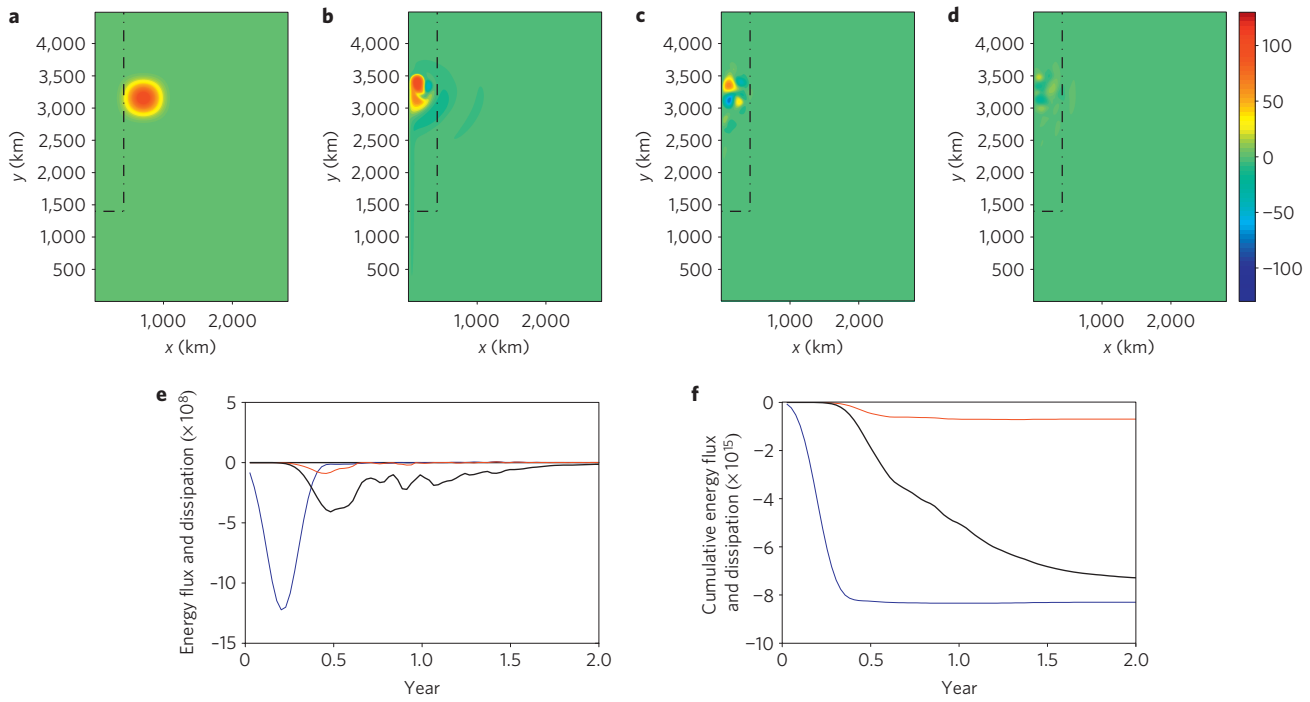

Figure 1 | Eddy energy budget for a single, anticyclonic eddy in the reduced-gravity model. a–d, The evolution of the layer-thickness anomaly (m) associated with the initial anticyclonic eddy at $t = 0$, 0.4, 1 and 2 years. The region near the western boundary enclosed by the dashed–dotted line is where the eddy energy-budget analysis is conducted. **e**, Time series of the zonal energy flux across the eastern open boundary (blue), meridional energy flux through the southern open boundary (red) and viscous dissipation within the selected region (black) (N m s^{-1}). **f**, Cumulative value of the curves in **e** (N m).

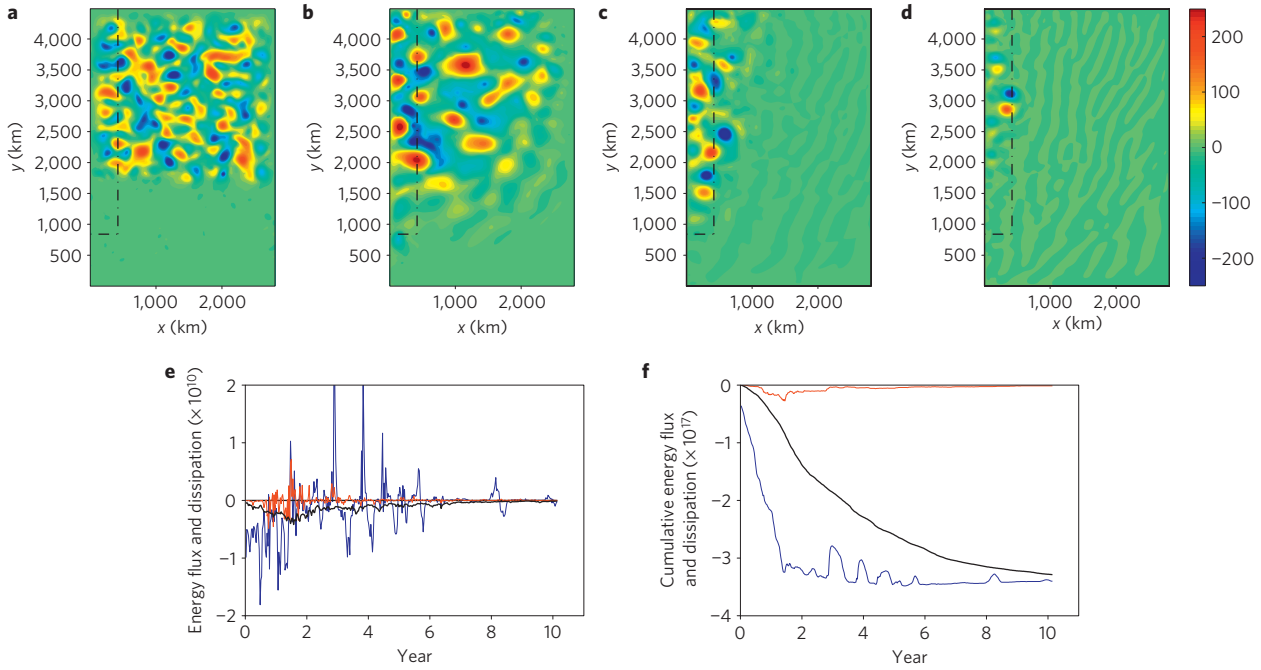

Figure 2 | Eddy energy budget for a sea of eddies in the reduced-gravity model. a–d, The evolution of the layer-thickness anomaly associated with the eddy field at $t = 0$, 0.8, 4 and 8 years. **e**,**f**, As in Fig. 1.

where $\mathbf{u}_1'$ and p_1' are the eddy geostrophic-velocity and pressure anomalies associated with the first baroclinic mode (see Methods). ∇_h is the horizontal gradient operator and z is the vertical coordinate. H is the water depth, which we assume varies slowly in space relative to the eddy energy flux. Figure 3 shows the 14-year average of the global divergence of eddy energy in the first baroclinic mode computed using the altimetry data and binned in 2° × 2° boxes. The most striking features are the ubiquitous eddy-energy divergence (in red) in the interior, and the eddy-energy convergence (in blue) near the western boundary in each ocean basin, representing sources and sinks of the first-baroclinic-mode eddy energy respectively. Some regional patterns of eddy-energy

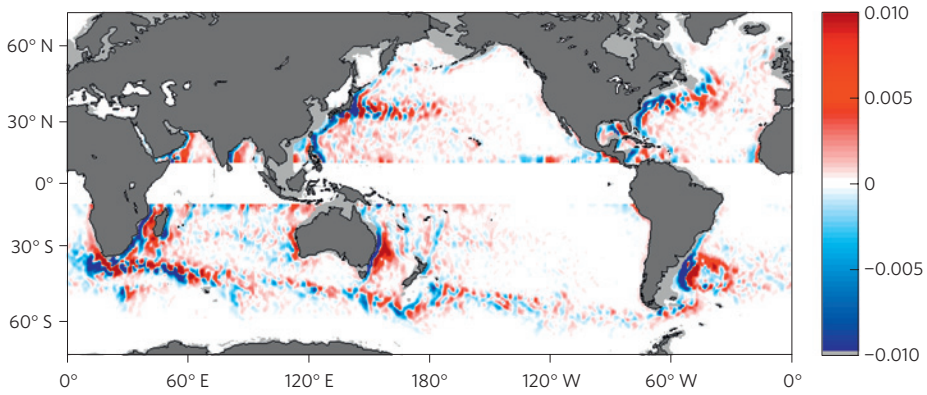

Figure 3 | Sources (red) and sinks (blue) of eddy energy in the first baroclinic mode. These are estimated using satellite altimetry and WOCE climatological data on the basis of (1) and binned in 2° × 2° boxes (W m^{-2}). Regions shallower than 300 m deep are shaded in light grey. Note the ubiquitous eddy-energy sinks (in blue) near the western boundary in each ocean basin. The colour scale is saturated to reveal regions of relatively moderate eddy-energy sources and sinks.

Table 1 | Estimated sink (in terawatts) of eddy energy in the first baroclinic mode near the western boundary.

Ocean basin	Altimetry + WOCE climatology		Altimetry + reduced-gravity model
	Linearized energy flux	Plus EKE	$H = 750$ m
North Atlantic	~0.022	~0.039	~0.034
South Atlantic	~0.018	~0.026	~0.015
North Pacific	~0.027	~0.041	~0.038
South Pacific	~0.015	~0.018	~0.028
North Indian	~0.011	~0.011	~0.019
South Indian	~0.046	~0.091	~0.048
Total	~0.14	~0.22	~0.19

The values are calculated poleward of 10° of latitude in each ocean basin from satellite altimetry and climatological data under different assumptions. Regions shallower than 300 m deep are excluded from our estimation.

sources and sinks are also intriguing. For example, in the North Atlantic there is an eddy-energy source immediately to the east of the New England Sea Mount and an eddy-energy sink in the slope region to the west. This is presumably associated with eddies generated through the Gulf Stream–New England Sea Mount interactions, their subsequent propagation to the west and ultimate dissipation along the sloping topography near the western boundary.

An animation of sea-surface-height anomalies (see Supplementary Information) reveals that, except in the Antarctic Circumpolar Current and separated Western Boundary Currents, eddies propagate ubiquitously westward and impinge on the sloping western boundary, where they disappear, as in the reduced-gravity model. In the reduced-gravity model, there is only one baroclinic mode and the only energy sink for eddies is lateral viscous dissipation. However, in the ocean, interaction with sloping bottom topography[6,15,16,19], energy transfer from geostrophic eddies to internal waves[13,14,17–19] and conversion to higher modes are also important. Regardless of the detailed mechanisms, both our model and the satellite altimetry data point to the western boundaries as an important region of energy loss for ocean eddies.

Using the altimetry data, we estimate the total eddy-energy convergence near the western boundaries poleward of 10° of latitude to be approximately 0.14 TW (see Methods). This represents a significant fraction of the 0.8 TW wind work on the extra-equatorial surface geostrophic motions[10–12,27]. The rate of eddy energy loss from the first baroclinic mode near the western boundaries in each ocean basin is listed in Table 1. We find that each hemisphere removes more or less the same amount of eddy energy, even though the majority of the wind energy input to the large-scale ocean circulation is found in the Southern Ocean[10–12,27]. To test the sensitivity of our estimates, we now diagnose the eddy-energy sink under different assumptions. If we relax the assumption of linearity in calculating the eddy energy flux and include the eddy kinetic energy, the energy sink increases by about 50% (see Table 1). An alternative is to use a reduced-gravity model, consistent with the numerical simulations, in which equation (1) becomes $D = \nabla_h \cdot (\rho g H \overline{\mathbf{u}'\eta'})$, where ρ is density. Assuming the eddy energy is ultimately dissipated, the total sink near the western boundaries is then about 0.2 TW if we choose $H = 750$ m, consistent with our numerical experiments (see Table 1). With a standard error of the mean of the order of 10% (see Methods), Table 1 yields a range of values from 0.12 to 0.25 TW for the eddy-energy sink. Given the uncertainties in the data we use, we estimate that the total eddy energy sink near the western boundaries poleward of 10° of latitude is approximately 0.1–0.3 TW.

Both theoretical arguments and numerical simulations show that, in the presence of ocean-like stratification, the efficiency of energy transfer from the first baroclinic mode to the barotropic mode is greatly reduced, leading to a concentration of eddy energy in the first baroclinic mode[24]. Dissipating eddies at the western boundary are consistent with this picture and provide a potential shortcut for removing energy input to the ocean, because the energy can be removed directly at the mesoscale through excitation of high-wavenumber vertical modes. This breaks the inverse energy cascade to larger horizontal and vertical scales in the ocean interior. Some of the dissipating processes may lead to enhanced diapycnal mixing in the western boundary regions[6]. Numerical

modelling studies suggest that the large-scale ocean circulation is sensitive to the spatial distribution of diapycnal mixing[28,29], and that boundary mixing is more effective at driving a vigorous meridional overturning circulation in the ocean[29]. Our results call for future research into the possibility, and the potential importance, of enhanced diapycnal mixing in the western boundary regions.

Methods

The nonlinear reduced-gravity model. The governing equations for the nonlinear reduced-gravity model are

$$\frac{\partial \mathbf{u}}{\partial t} + (f+\xi)\mathbf{k}\times\mathbf{u} + \nabla B = K_h\nabla^2\mathbf{u} \tag{2}$$

$$\frac{\partial h}{\partial t} + \nabla\cdot(h+H)\mathbf{u} = 0 \tag{3}$$

where $\xi = \partial v/\partial x - \partial u/\partial y$ is the relative vorticity, $B = g'h + (u^2+v^2)/2$ is the Bernoulli potential, g' is the reduced gravity, H is the mean layer thickness, h is the layer-thickness anomaly associated with the eddies, f is the Coriolis parameter, $\mathbf{k}$ is a unit vertical vector, K_h is the lateral viscosity coefficient and t is time. The energy equation is derived by $\rho(h+H)\mathbf{u}\times$ (2) $+ \rho B\times$ (3) such that

$$\begin{aligned}\frac{\partial E}{\partial t} &= -\rho\nabla\cdot((h+H)\mathbf{u}B)\\ &- \rho(h+H)K_h[|\nabla u|^2+|\nabla v|^2]\\ &+ \frac{1}{2}\rho(h+H)K_h\nabla^2(u^2+v^2)\end{aligned} \tag{4}$$

where $E = (1/2)\rho(h+H)(u^2+v^2) + (1/2)\rho g'h^2$ is the total eddy energy. The terms on the right-hand side of equation (4) are the zonal and meridional energy fluxes, viscous dissipation of eddy kinetic energy and horizontal diffusion of eddy kinetic energy. No eddy-generation terms are included in (4) because we are only concerned with the fate of pre-existing eddies.

Now consider a region of interest enclosed by the dashed–dotted line near the western boundary in Fig. 1a. Integrating (4) over this region and ignoring the diffusive transport of eddy kinetic energy across the open boundaries (which is extremely small), we obtain

$$\begin{aligned}\frac{\partial}{\partial t}\int E\,\mathrm{d}S \approx &\underbrace{-\rho\int((h+H)uB)\mathrm{d}y}_{\text{zonal energy flux}} + \underbrace{\rho\int((h+H)vB)\mathrm{d}x}_{\text{meridional energy flux}}\\ &\underbrace{-\rho\int((h+H)K_h[|\nabla u|^2+|\nabla v|^2])\mathrm{d}S}_{\text{viscous energy dissipation}}\end{aligned} \tag{5}$$

where S is the surface area of the selected region. In physical terms, equation (5) states that the change of eddy energy within the control volume is caused by eddy energy flux from the east, energy flux through the southern open boundary and viscous removal of eddy energy within the volume.

Interpreting the eddy-energy divergence using the reduced-gravity model. The eddy energy flux from (5) is

$$\overline{\rho(h+H)\mathbf{u}B} \approx \rho g H\overline{\mathbf{u}'\eta'}$$

when linearized about a state of rest, where an overbar represents time-averaging and g is the acceleration due to gravity. The sea-surface-height anomaly, η', has been related to the layer-thickness anomaly through $g\eta' \approx g'h$. Substituting $\mathbf{u}' = (g/f)\mathbf{k}\times\nabla_h\eta'$ into $D = \nabla_h\cdot(\rho g H\overline{\mathbf{u}'\eta'})$, we get

$$D = -\frac{\rho g^2\beta}{f^2}\frac{\partial}{\partial x}\left(H\frac{\overline{\eta'^2}}{2}\right) \approx -\frac{\partial}{\partial x}\left(\frac{1}{2}c_R\rho g'\overline{h^2}\right) \tag{6}$$

where $c_R = g'H\beta/f^2$ is the long-Rossby-wave speed[5]. Provided that $\overline{\eta'^2}$ is small at the ocean boundaries, as observed[21], it follows from (6) that D can be interpreted as the divergence of eddy energy that propagates at long-Rossby-wave speeds. See Supplementary Information for the surface-height-anomaly variance ($\overline{\eta'^2}$) in the global ocean.

Eddy-energy divergence using altimetry and hydrographic data. Under the hydrostatic and Boussinesq approximations and for an ocean of constant depth H, the pressure eigenmodes $\hat{p}_n(z)$ are solutions to

$$\frac{\mathrm{d}}{\mathrm{d}z}\left(\frac{1}{N^2}\frac{\mathrm{d}}{\mathrm{d}z}\hat{p}_n\right) + \frac{1}{c_n^2}\hat{p}_n = 0$$

subject to the boundary conditions

$$\frac{\mathrm{d}\hat{p}_n}{\mathrm{d}z} = 0 \text{ at } z = -H$$

and

$$\frac{\mathrm{d}\hat{p}_n}{\mathrm{d}z} = -\frac{N^2\hat{p}_n}{g} \text{ at } z = 0$$

c_n are the eigenspeeds and N is the buoyancy frequency. Assuming that the altimetry data reflect mostly the first baroclinic mode in the open ocean[23,24], that is, $p_1'(x,y,0,t) = \rho g\eta'$, we obtain the pressure anomaly at depth associated with the first baroclinic mode

$$p_1'(x,y,z,t) = \rho g\eta'\frac{\hat{p}_1(x,y,z)}{\hat{p}_1(x,y,0)} \tag{7}$$

where $\hat{p}_1(x,y,z)$ is the mode structure at each location. The baroclinic eddy-energy-flux divergence is computed using the covariance of the mode 1 velocity and baroclinic pressure anomaly, assuming that H varies slowly in space relative to eddy energy flux,

$$D = \nabla_h\cdot\left(\int_{-H}^{0}\overline{\mathbf{u}_1'p_1'}\mathrm{d}z\right) = -\int_{-H}^{0}\frac{\beta}{2f^2\rho}\frac{\partial\overline{p_1'^2}}{\partial x}\mathrm{d}z \tag{8}$$

Substituting (7) into (8), we get

$$D = -\frac{\rho g^2\beta}{2f^2}\frac{\partial}{\partial x}\left(\frac{\int_{-H}^{0}\hat{p}_1^2(x,y,z)\mathrm{d}z}{\hat{p}_1^2(x,y,0)}\overline{\eta'^2}\right)$$

We then sum up the eddy-energy sink near the western boundary poleward of 10° of latitude in each ocean basin.

Errors. There are limitations with our analysis of the eddy-energy divergence using altimetry data. The satellite tracks are widely spaced relative to mesoscales in the ocean, and the gridded altimetry dataset is subject to spatial and temporal averaging. This will inevitably underestimate mesoscale variabilities in the ocean. Measurements derived from altimetry near the coast have to be viewed with caution, as standard tidal and atmospheric corrections may have larger errors than offshore. However, a decrease of sea-surface-height variability close to the western boundary is a robust feature in both *in situ* measurements[21] and eddy-resolving numerical models[30]. Furthermore, there is a sharper decrease of dynamic height variability towards the western boundary in mooring measurements than the gridded altimetry dataset can resolve[21]. In addition, we exclude regions shallower than 300 m deep in our calculation.

The standard error of the mean is estimated using $s/\sqrt{n}$, where s is the standard deviation, and n is the number of independent observations. The standard error of the mean for the eddy-energy sink ranges from 5 to 18% for a reasonable range of decorrelation timescales between 1 week and 3 months.

Received 6 April 2010; accepted 26 July 2010; published online 22 August 2010

References

1. Gill, A. E., Green, J. S. A. & Simmons, A. J. Energy partition in the large-scale ocean circulation and the production of mid-ocean eddies. *Deep-Sea Res.* **21,** 499–528 (1974).
2. Smith, K. S. Eddy amplitudes in baroclinic turbulence driven by nonzonal mean flow: Shear dispersion of potential vorticity. *J. Phys. Oceanogr.* **37,** 1037–1050 (2007).
3. Ferrari, R. & Wunsch, C. Ocean circulation kinetic energy: Reservoirs, sources, and sinks. *Annu. Rev. Fluid Mech.* **41,** 253–282 (2009).
4. Wunsch, C. & Ferrari, R. Vertical mixing, energy, and the general circulation of the oceans. *Annu. Rev. Fluid Mech.* **36,** 281–314 (2004).
5. Chelton, D. B., Schlax, M. G., Samelson, R. M. & de Szoeke, R. A. Global observations of large oceanic eddies. *Geophys. Res. Lett.* **34,** L15606 (2007).
6. Dewar, W. K. & Hogg, A. M. Topographic inviscid dissipation of balanced flow. *Ocean Modelling* **32,** 1–13 (2010).
7. Sen, A., Scott, R. B. & Arbic, B. K. Global energy dissipation rate of deep-ocean low-frequency flows by quadratic bottom boundary layer drag: Computations from current-meter data. *Geophys. Res. Lett.* **35,** L09606 (2008).
8. Duhaut, T. H. & Straub, D. N. Wind stress dependence on ocean surface velocity: Implications for mechanical energy input to ocean circulation. *J. Phys. Oceanogr.* **36,** 202–211 (2006).
9. Zhai, X. & Greatbatch, R. J. Wind work in a model of the northwest Atlantic Ocean. *Geophys. Res. Lett.* **34,** L04606 (2007).
10. Hughes, C. W. & Wilson, C. Wind work on the geostrophic ocean circulation, including effects of small scales in the wind stress. *J. Geophys. Res.* **113,** C02016 (2008).
11. Xu, Y. & Scott, R. B. Subtleties in forcing eddy resolving ocean models with satellite wind data. *Ocean Modelling* **20,** 240–251 (2008).

12. Scott, R. B. & Xu, Y. An update on the wind power input to the surface geostrophic flow of the world ocean. *Deep-Sea Res.* **56,** 295–304 (2009).
13. Molemaker, M. J., McWilliams, J. C. & Yavneh, I. Baroclinic instability and loss of balance. *J. Phys. Oceanogr.* **35,** 1505–1517 (2005).
14. Bühler, O & McIntyre, M. E. Wave capture and wave vortex duality. *J. Fluid Mech.* **534,** 67–95 (2005).
15. Holloway, G. Representing topographic stress for large-scale ocean models. *J. Phys. Oceanogr.* **22,** 1033–1046 (1992).
16. Adcock, S. T. & Marshall, D. P. Interactions between geostrophic eddies and the mean circulation over large-scale bottom topography. *J. Phys. Oceanogr.* **30,** 3223–3238 (2000).
17. Polzin, K. & Firing, E. Estimates of diapycnal mixing using LADCP and CTD data from I8S. *Int. WOCE Newslett.* **29,** 39–42 (1997).
18. Marshall, D. P. & Naveira Garabato, A. C. A conjecture on the role of bottom-enhanced diapycnal mixing in the parameterization of geostrophic eddies. *J. Phys. Oceanogr.* **38,** 1607–1613 (2008).
19. Nikurashin, M. & Ferrari, R. Radiation and dissipation of internal waves generated by geostrophic motions impinging on small-scale topography: Theory. *J. Phys. Oceanogr.* **40,** 1055–1074 (2010).
20. Johnson, H. L. & Marshall, D. P. A theory for the surface Atlantic response to thermohaline variability. *J. Phys. Oceanogr.* **32,** 1121–1132 (2002).
21. Kanzow, T. *et al*. Observing basin-wide integrated volume transports in an eddy-filled ocean. *J. Phys. Oceanogr.* **39,** 3091–3110 (2009).
22. Pedlosky, J. A study of the time dependent ocean circulation. *J. Phys. Oceanogr.* **22,** 267–272 (1965).
23. Wunsch, C. The vertical partition of oceanic horizontal kinetic energy. *J. Phys. Oceanogr.* **28,** 1770–1794 (1997).
24. Smith, K. S. & Vallis, G. K. The scales and equilibration of midocean eddies: Freely evolving flow. *J. Phys. Oceanogr.* **31,** 554–571 (2001).
25. Le Traon, P. Y., Nadal, F. & Ducet, N. An improved mapping method of multisatellite altimeter data. *J. Atmos. Oceanic Technol.* **15,** 522–534 (1998).
26. Gouretski, V. V. & Koltermann, K. P. *WOCE Global Hydrographic Climatology*. Ber. Bundesamte Seeschifffahrt Hydrogr. Rep. 35 (Bundesamt Seeschiffahrt Hydrogr., 2004).
27. Wunsch, C. The work done by the wind on the oceanic general circulation. *J. Phys. Oceanogr.* **28,** 2332–2340 (1998).
28. Samelson, R. M. Large-scale circulation with locally enhanced vertical mixing. *J. Phys. Oceanogr.* **28,** 712–726 (1998).
29. Scott, J. R. & Marotzke, J. The location of diapycnal mixing and the meridional overturning circulation. *J. Phys. Oceanogr.* **32,** 3578–3595 (2002).
30. Maltrud, M. E. & McClean, J. L. An eddy resolving global 1/10° ocean simulation. *Ocean Modelling* **8,** 31–54 (2005).

Acknowledgements

We are grateful for funding from the UK Natural Environment Research Council. H.L.J. is supported by a Royal Society University Research Fellowship and D.P.M. acknowledges additional support from the James Martin 21st Century School, University of Oxford.

Author contributions

X.Z. conducted the numerical experiments and analysis of the altimetry data. All the authors contributed to design of the study, interpretation of the results and writing of the manuscript.

Additional information

The authors declare no competing financial interests. Supplementary information accompanies this paper on www.nature.com/naturegeoscience. Reprints and permissions information is available online at http://npg.nature.com/reprintsandpermissions. Correspondence and requests for materials should be addressed to X.Z.